Chinese Chemical Letters 37 (2026) 111724

Contents lists available at ScienceDirect

Chinese Chemical Letters

journal homepage: www.elsevier.com/locate/cclet

# Ultrathin Pd based bimetallic nanowires as highly efficient ampere-level pH-universal water splitting

Yuanwei Ma[a,1], Jigang Wang[a,1], Zhaodi Yan[a,1], Qiang Liu[a], Lanyan Li[b,*], Zhongfang Li[a], Likai Wang[a,c,d,*]

[a] School of Chemistry and Chemical Engineering, Shandong University of Technology, Zibo 255049, China
[b] School of Resources and Environment, Hunan University of Technology and Business, Changsha 410205, China
[c] School of Chemical and Biological Engineering, and Institute of Chemical Process, Seoul National University, Seoul 08826, Republic of Korea
[d] Key Laboratory of Advanced Energy Materials Chemistry (Ministry of Education), Nankai University, Tianjin 300071, China

ARTICLE INFO

*Article history:*
Received 20 February 2025
Revised 14 August 2025
Accepted 14 August 2025
Available online 14 August 2025

*Keywords:*
PdPt
Alloy
Nanowires
Water splitting
HER

ABSTRACT

Herein, we have developed a straightforward wet-chemical method to synthesize a series of Pd-based alloy nanowires (NWs), including PdPt NWs, PdAu NWs, PdIr NWs, and PdRu NWs, which exhibits high mass activity and turnover frequency (TOF) for HER, surpassing Pt/C by 4.6-fold and 1.5-fold in acidic and alkaline electrolytes, respectively. It also demonstrates high stability in alkaline electrolyte at a current density of 220 mA/cm$^2$ for 280 h, highlighting its potential for practical applications under industrial current conditions. PdPt NWs exhibited ultrathin structures with head-to-tail kinks and inherent defects, significantly increasing the density of active sites and precisely tuning the electronic structure, which could accelerate reaction kinetics and boost water-splitting electrocatalytic performance. This study highlights the potential of PdPt NWs as highly efficient catalysts, offering outstanding catalytic performance and stability for practical applications.

© 2025 Published by Elsevier B.V. on behalf of Chinese Chemical Society and Institute of Materia Medica, Chinese Academy of Medical Sciences.

With the rapid advancement of economic society, fossil fuel reserves are swiftly depleting, prompting the development of clean energy to solve the global energy crisis. Hydrogen acts as an ideal clean energy source due to high energy density, environmentally friendly, and non-toxic by-products [1–3]. Electrochemical water splitting is an especially promising route for hydrogen production, including the hydrogen evolution reaction (HER) at the cathode and oxygen evolution reaction (OER) at the anode [4–9]. However, the slow reaction kinetics and high energy barriers limit their practical applications. To overcome these challenges, extensive research has been dedicated to developing advanced electrocatalysts. Pt/C demonstrates outstanding HER activity [10–23], while Ru/Ir oxides remain the most efficient electrocatalysts for OER in electrochemical water splitting [24,25].

Alloying metals has emerged as one of the most effective strategies for altering the chemical composition and physical properties of materials, enabling the optimization of their catalytic performance by fine-tuning electronic structures [26–28]. Among them, palladium (Pd) stands out as a highly promising alternative to platinum (Pt) due to its similar lattice structure and parameters. Pd-based bimetallic nanostructures have been extensively explored and developed as catalytic materials [29–35]. Various morphologies of Pd-based bimetallic nanostructures, including nanosheet [6,36,37], nanotube [38,39], nanowires [40–42], and nanocube [43,44], have exhibited exceptional catalytic properties. These alloyed microstructures can not only enhance catalytic activity but also contribute to reducing Pt consumption. In the pursuit of high-efficiency electrocatalysts, the precise control of metal material structures enables the fine adjustment of surface morphology and composition, leading to enhanced and even novel catalytic activity [45,46]. One-dimensional (1D) metal nanowires (NWs) possess unique advantages, including intrinsic anisotropic morphology, excellent flexibility, high surface-to-volume ratio, and enhanced electrical conductivity. These characteristics have been widely leveraged in diverse electrocatalytic reactions, significantly demonstrating superior performance compared to their isotropic nanoparticle (NP) counterparts [40,47–51]. However, conventional Pd-based alloy nanowires with relatively large diameters and smooth surfaces frequently exhibit weaker electronic interactions, which are crucial for maximizing electrocatalytic efficiency. But ultrathin Pd-based alloy nanowires could offer an increased number of active

* Corresponding authors.
*E-mail addresses:* lly820@hotmail.com (L. Li), lkwangchem@sdut.edu.cn (L. Wang).
[1] These authors contributed equally to this work.

https://doi.org/10.1016/j.cclet.2025.111724
1001-8417/© 2025 Published by Elsevier B.V. on behalf of Chinese Chemical Society and Institute of Materia Medica, Chinese Academy of Medical Sciences.

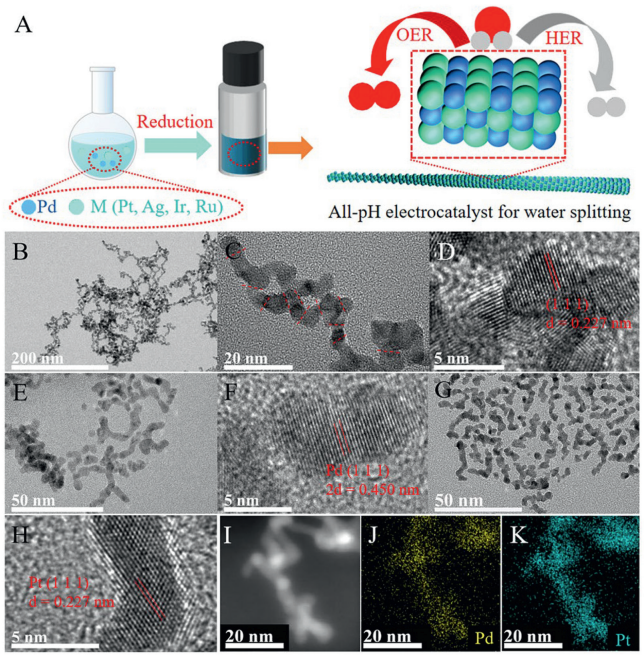



**Fig. 1.** (A) The typical synthetic route for preparing PdPt NWs. (B, C) TEM images and (D) corresponding HR-TEM image of PdPt-2 NWs. (E) High magnification of TEM image and (F) corresponding HR-TEM image of Pd NWs. (G) High magnification of TEM image and (H) corresponding HR-TEM image of Pt NWs. (I) HAADF-STEM image of PdPt-2 NWs, and corresponding elemental mapping images of (J) Pd and (K) Pt.

sites, thereby enhancing catalytic activity. In this study, we present a simple wet-chemical approach for synthesizing a series of Pd-based alloy nanowires, including PdPt, PdAu, PdIr, and PdRu NWs. Among these, PdPt NWs exhibit remarkable HER activity across a wide pH range, achieving the lowest overpotential for water splitting in 1.0 mol/L KOH, 0.5 mol/L $H_2SO_4$, and 1.0 mol/L PBS, respectively. This study highlights the potential of PdPt NWs as highly efficient catalysts, providing exceptional catalytic performance and stability for practical applications.

As depicted in Fig. 1A, the fabrication of PdPt NWs is operated by a straightforward wet-chemical method using $PdCl_2$ and $H_2PtCl_6$ as metal precursors with $KBH_4$ as the reducing agent and TX-114 served as the template. Typically, $PdCl_2$ and $H_2PtCl_6$ were dissolved and mixed in an ice-water bath, followed by the addition of TX-114 to the prepared solution. Subsequently, a freshly prepared $KBH_4$ solution was introduced to the mixture and stirred continuously for 1.5 h, resulting in the formation of PdPt nanowires (NWs), which were then further analyzed. Similarly, PdIr NWs, PdRu NWs, and PdAu NWs were fabricated with the same procedure by substituting $H_2PtCl_6$ with $IrCl_3$, $RuCl_3$, and $HAuCl_4$, respectively. Detailed information can be found in Table S1 (Supporting information). The metal content was detected by ICP-MS, and the results are similar to the initial theoretical ratio (Table S2 in Supporting information).

The morphology of PdPt-2 NWs is shown in Fig. 1B, where the representative TEM image distinctly reveals their uniform size and pure morphology. From Fig. 1C, high magnification TEM image further demonstrates PdPt-2 NWs featured ultrathin wire-like structures *via* head-to-tail kinks with the average diameter of only 5 nm and extending to the length of several hundred nanometers. The nanowires also displayed some defects, such as, atomic kinks, edge sites, and grain boundaries. Additionally, high-resolution TEM (HR-TEM) displayed distinct lattice fringes with the D-spacing of 0.227 nm in Fig. 1D, corresponding to the (111) plane of a face-centered cubic (*fcc*) PdPt alloy. The selected electron diffraction (SAED) patterns (Fig. S1 in Supporting information) further confirms that PdPt NWs exhibits a well-defined crystalline nanostructure, as indicated by the presence of sharp diffraction rings, which could be attributed to the (111), (200), (220), (331) and (222) lattice planes of Pt and Pd [52]. The rings from Pt and Pd almost overlap due to the slight differences in the lattice parameters. Pd NWs demonstrates ultrathin 1D structure as depicted in Figs. 1E and F also presents a lattice spacing of Pd (0.225 nm), a slightly decreased further compared to that of PdPt NWs (0.227 nm). But Pt NWs only exhibits some short nanowires in Fig. 1G. As shown in Fig. 1H, the lattice spacing of Pt is measured to be 0.227 nm [53], further indicating that Pd is successfully alloyed with Pt. The morphological difference between Pd and Pt NWs may be attributed to the sequential reduction of $Pd^{2+}$ and $Pt^{2+}$ by $KBH_4$. The successful fabrication of bimetallic PdPt NWs is further validated by HAADF-STEM in Fig. 1I, the distribution of Pd and Pt elements (Figs. 1J and K) is uniformly throughout the nanowire structure, suggesting the successful formation of bimetallic PdPt alloy. Additionally, a series of Pd-based alloy NWs could be fabricated by replacing Pt with Au, Ru and Ir, including PdAu NWs, PdRu NWs, and PdIr NWs. From Figs. S2-S4 (Supporting information), TEM images demonstrated the highly dispersed structures of PdAu, PdRu, and PdIr nanowires, respectively, confirming the viability of the fabrication strategy.

X-ray diffraction (XRD) was employed to further examine the crystallinity of PdPt NWs. As shown in Fig. 2A, the diffraction peaks of Pd NWs can be assigned to *fcc* Pd pattern appearing at 40.0°, 46.6°, 68.0°, and 82.0°, corresponding to the (111), (200), (220), and (311) planes of Pd (PDF #46–1043) [51,54,55]. In comparison of Pd NWs, a slight negative shift (~0.2°) towards lower degree was observed in PdPt-2 NWs, which might be ascribed to the smaller atomic radius of Pd compared to that of Pt, further indicating the formation of PdPt alloy. Similar results are presented in Fig. S5A (Supporting information), where XRD patterns (Fig. S6 in Supporting information) of PdIr NWs display peaks around 40°, corresponding to *fcc* Pd (111), confirming the formation of PdIr. To further examine the electronic structure and valence states of the elements in PdPt NWs, X-ray photoelectron spectroscopy (XPS) analysis was also investigated. From Fig. 2B and Fig. S5B (Supporting information), the survey XPS spectra of PdPt NWs revealed the presence of Pd and Pt, and high-resolution XPS spectra of Pd 3d and Pt 4f also confirmed the synthesis of PdPt NWs. As depicted in Fig. 2C and Fig. S5C (Supporting information), the peaks at 335.75 and 341.20 eV could be attributed to $Pd^0$ $3d_{5/2}$ and $Pd^0$ $3d_{3/2}$, respectively, while the peaks located at 336.90 and 342.75 eV were assigned to $Pd^{2+}$ $3d_{5/2}$ and $Pd^{2+}$ $3d_{3/2}$ [56,57]. Compared to Pd NWs, Pd 3d spectra of PdPt-2, PdPt-4 and PdPt-5 NWs exhibited a positive shift to higher binding energy (BE). Notably, the shift of Pd $3d_{3/2}$ and $3d_{5/2}$ became more pronounced as the Pd content increased. As displayed in Fig. 2D and Fig. S5D (Supporting information), the peaks at 71.90 and 75.13 eV were attributed to $Pt^0$ $4f_{7/2}$ and $Pt^0$ $4f_{5/2}$, respectively, and there were also other two peaks of at 71.55 and 74.90 eV assigned to $Pt^{2+}$. The BE of Pt 4f in PdPt NWs showed a significant negative shift compared to that of Pt NWs, this shift is likely due to the difference in electronegativity between Pd (2.20) and Pt (2.28), resulting in the electron transfer from Pd to Pt [40,58]. Obviously, the BE of Pd and Pt were shifted relative to those of metallic Pd and Pt, which indicated a weaker binding strength of intermediate species on Pd and Pt sites, thereby boosting electrocatalytic activity. Furthermore, X-ray absorption fine structure (XAFS) analysis was also performed to investigate the electronic and atomic structures of Pt and Pd in PtPd-2 NWs. The X-ray absorption near-edge structure (XANES) spectrum at the Pt L3-edge (Fig. 2E) reveals that Pt in PtPd-2 NWs predominantly exists in a metallic state. The Fourier-transformed (FT) EXAFS spectrum of Pt in PtPd-2 NWs (Fig. 2F) exhibits distinct

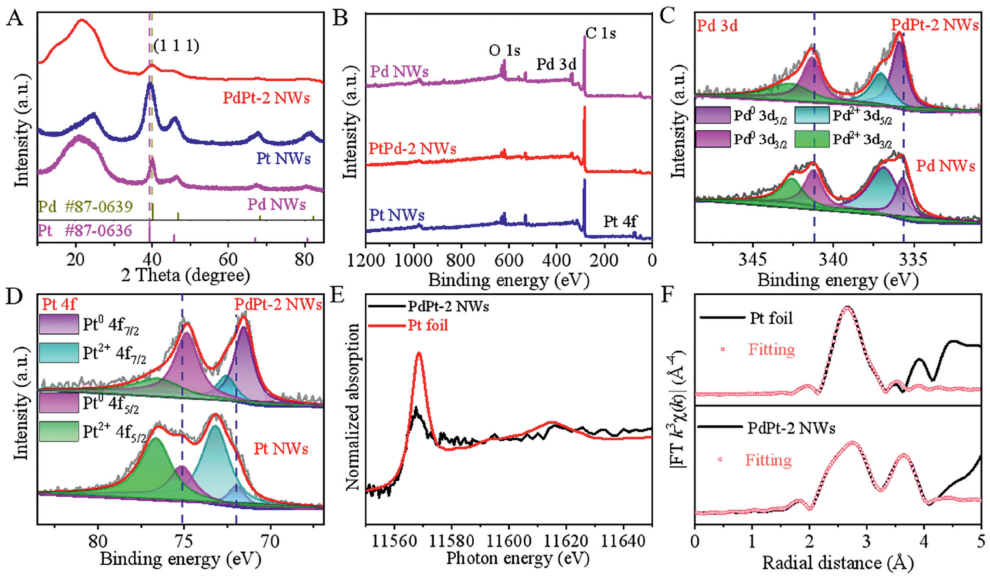



**Fig. 2.** (A) XRD patterns of PdPt-2 NWs, Pt NWs, and Pd NWs. (B) XPS survey spectra of Pd NWs, PdPt-2 NWs, and Pt NWs. (C) High-resolution XPS Pd 3d spectra of Pd NWs and PdPt-2 NWs. (D) High-resolution XPS Pt 4f spectra of PdPt-2 and Pt NWs. (E) XANES and (F) FT-EXAFS curves of PdPt-2 NWs and Pt foil.

backscattering peaks at 2.70 Å, corresponding to Pt-Pd/Pt bonds, respectively [59,60].

To explore their electrocatalytic performance, PdPt NWs were investigated in a three-electrode system across a full range of pH. As illustrated in Fig. S7 (Supporting information), the HER activity was first assessed in $N_2$-saturated 0.5 mol/L $H_2SO_4$, revealing that PdPt-2 NWs exhibited the most favorable performance, characterized by the smallest overpotential, the smallest Tafel slope, the minimal $\Delta\eta/\Delta\log|j|$ ratio, higher potential-dependent TOF, and the lowest charge transfer resistance ($R_{ct}$) among all tested PdPt NWs.

From Fig. 3A, HER LSV curves of PdPt-2 NWs, Pd NWs, Pt NWs, and Pt/C catalysts were measured at a sweep rate of 5 mV/s, it was evident that PdPt-2 NWs exhibited the highest HER activity, requiring an overpotential of 218 mV to achieve a current density of 500 mA/cm$^2$ (Fig. 3B), significantly surpassing that of Pd NWs (572 mV), Pt NWs (506 mV), Pt/C (328 mV). The intrinsic reaction kinetics of the HER process remains a vital parameter for evaluating the efficiency of electrocatalysts. To reveal the HER kinetics, the $\Delta\eta/\Delta\log|j|$ ratios were also performed and evaluated in 0.5 mol/L $H_2SO_4$ in Fig. 3C, where $\eta$ represents the overpotential and $j$ denotes the current density. Notably, the Pt/C electrode exhibited an increasing $\Delta\eta/\Delta\log|j|$ value as the current density reached 2 A/cm$^2$, with a $\Delta\eta/\Delta\log|j|$ of 380.1 mV/dec at the range of 400–800 mA/cm$^2$, while the PdPt-2 NWs remained 324.5 mV/dec, implying significantly enhanced HER kinetics. Turnover frequencies (TOFs) were calculated to assess the intrinsic activities of PdPt-2 NWs, Pd NWs, Pt NWs and Pt/C in Figs. 3D and B. The results demonstrated that PdPt-2 NWs exhibited an exceptionally high TOF value of 38.11 s$^{-1}$ at $\eta_{150}$, outperforming Pd NWs (1.61 s$^{-1}$), Pt NWs (2.36 s$^{-1}$), and Pt/C (8.19 s$^{-1}$), implying its exceptional intrinsic HER activity in 0.5 mol/L $H_2SO_4$. Furthermore, to gain the deeper insights into the electrocatalytic performance, the mass activity of PdPt-2 NWs was found to be remarkably higher, reaching 18.9 A/mg$_{Pt}$ at 200 mV compared to Pt/C (2.5 A/mg$_{Pt}$) in Fig. 3E. The Tafel slopes for PdPt-2 NWs, Pd NWs, Pt NWs and Pt/C catalysts were determined to be 41.5, 213.8, 156.5, and 43.3 mV/dec in Figs. 3F and B, respectively, indicating that PdPt-2 NWs exhibit faster electrocatalytic HER kinetics. Moreover, electrochemical impedance spectroscopy (EIS) tests revealed that PdPt-2 NWs had the lowest $R_{ct}$ in comparision of Pd NWs, Pt NWs and Pt/C in Fig. 3G, suggesting the incorporation of Pt and Pd could promote electron transfer, superior conductivity and less energy-consuming, thereby boosting HER activity. For practical applications, a pH-universal catalytic response is essential, the electrochemical properties of as-prepared samples were further investigated in $N_2$-saturated 1 mol/L KOH and 1 mol/L PBS, respectively.

As depicted in Figs. S8-S11 (Supporting information), PdPt-2 NWs demonstrated the superior performance, characterized by the lowest overpotential, the smallest Tafel slope, minimal $\Delta\eta/\Delta\log|j|$ ratio, higher Potential-dependent TOF, and the smallest $R_{ct}$ among all PdPt NWs. The LSV curves in Fig. 3H exhibit the HER activity of PdPt-2 NWs, Pd NWs, Pt NWs and Pt/C in 1 mol/L KOH, PdPt-2 NWs required only 442 mV of overpotential to achieve a current density of 500 mA/cm$^2$, superior to that of Pd NWs (860 mV) and Pt NWs (643 mV), and Pt/C (462 mV) in Fig. S8F. From Fig. S8A, Tafel plots of PdPt-2 NWs, Pd NWs, Pt NWs, and Pt/C were also estimated to be 102.2 mV/dec, 380.4 mV/dec, 306.2 mV/dec, and 150.3 mV/dec, respectively, suggesting that PdPt-2 NWs exhibited the fastest electrocatalytic HER kinetics [61,62]. To reveal the HER kinetics of catalysts, the $\Delta\eta/\Delta\log|j|$ ratio was performed and evaluated in 1 mol/L KOH in Fig. S8B. PdPt-2 NWs maintained a significantly lower value of 614.6 mV/dec than that of Pt/C (1042.2 mV/dec), confirming its ultrafast HER kinetics. Furthermore, PdPt-2 NWs exhibited a higher mass activity (8.45 A/mg$_{Pt}$ at 200 mV) than Pt/C (2.75 A/mg$_{Pt}$ at 200 mV) in Fig. S8C. At $\eta_{150}$, PdPt-2 NWs displayed a TOF of 33.43 s$^{-1}$, far surpassing Pt NWs (31.30 s$^{-1}$), Pd NWs (1.61 s$^{-1}$), and Pt/C (21.91 s$^{-1}$), indicating its superior intrinsic HER activity in 1 mol/L KOH (Fig. S8D). Additionally, PdPt-2 NWs had the lowest $R_{ct}$ among all tested samples (Fig. S8E). HER activity of PdPt-2 NWs was further examined in 1 mol/L PBS in Fig. 3I, and the LSV curves (Fig. S10F) show that PdPt-2 NWs achieved the overpotential of 742 mV at 500 mA/cm$^2$, outperforming that of Pd NWs (1184 mV), Pt NWs (976 mV), and even commercial Pt/C (865 mV). From Fig. S10A, Tafel slope of PdPt-2 NWs, Pd NWs, Pt NWs, and Pt/C were 150.2, 590.4, 501.7, and 220.3 mV/dec, respectively, implying the superior electrocatalytic HER kinetics of PdPt-2 NWs. Moreover, the $\Delta\eta/\Delta\log|j|$ ratio, mass activity, TOF, and EIS tests were also analysed, suggesting that the alloy of PdPt could boost HER activity (Fig. S10). Electrochemical surface area (ECSA) is another essential parameter for evaluating catalytic performance. As shown in Figs. S12 and S13 (Supporting

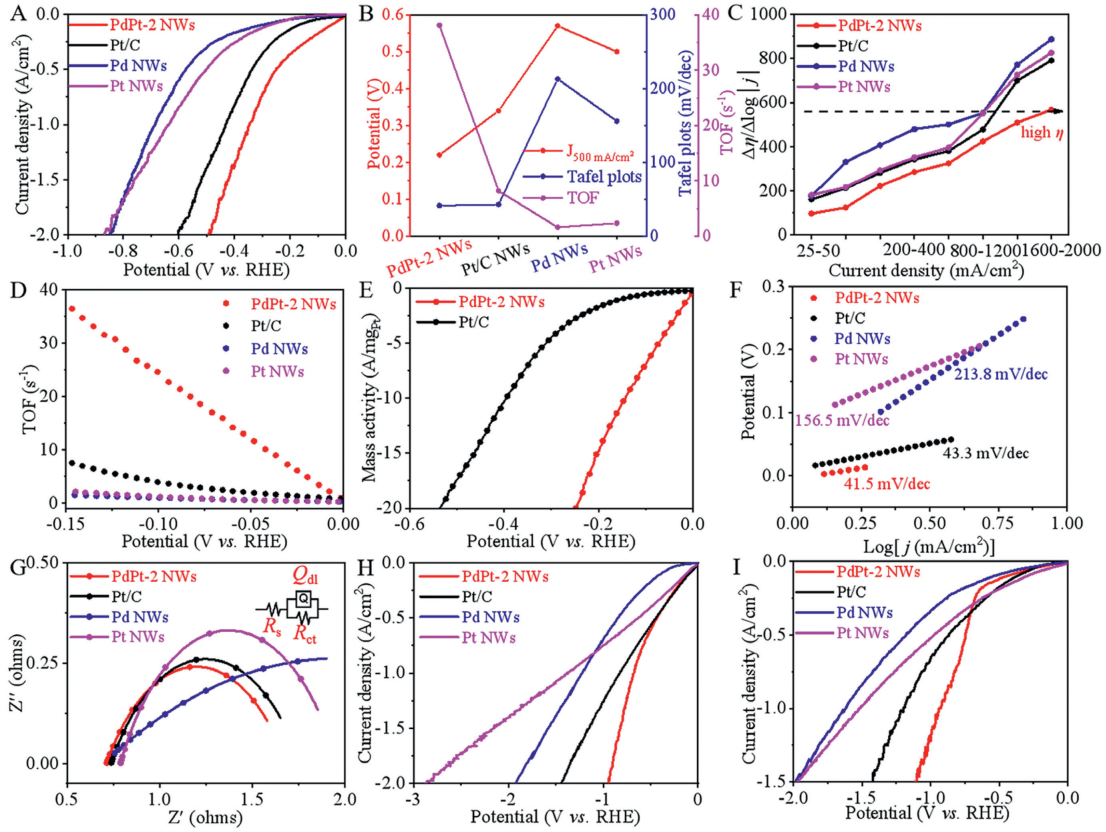



**Fig. 3.** (A) LSV curves of PdPt-2 NWs, Pd NWs, Pt NWs and Pt/C in 0.5 mol/L $H_2SO_4$. (B) plot of current density at 500 mA/cm$^2$, TOF and Tafel slope . (C) $\Delta\eta/\Delta\log|j|$ ratios of PdPt-2 NWs, Pd NWs, Pt NWs and Pt/C in 0.5 mol/L $H_2SO_4$. (D) Potential-dependent turnover frequency (TOF) curves in 0.5 mol/L $H_2SO_4$. (E) Mass activity curves of PdPt-2 NWs and Pt/C in 0.5 mol/L $H_2SO_4$. (F) Tafel plots of PdPt-2 NWs and Pt/C in 0.5 mol/L $H_2SO_4$. (G) Electrochemical impedance spectra of PtPd-2 NWs, Pd NWs, Pt NWs and Pt/C in 0.5 mol/L $H_2SO_4$. The equivalent circuit used to fit the EIS data is illustrated in the inset ($R_s$, solution resistance; $R_{ct}$, charge-transfer resistance; $Q_{dl}$, constant phase element for the double layer). (H) LSV curves of PdPt-2 NWs, Pd NWs, Pt NWs and Pt/C in 1 mol/L KOH. (I) LSV curves of PdPt-2 NWs, Pd NWs, Pt NWs and Pt/C in 1 mol/L PBS.

information), ECSA of PdPt-2 NWs, Pd NWs, Pt NWs, and Pt/C are 44.7, 1.50, 18.1 and 15.8 m$^2$/g, respectively. Among PdPt NWs catalysts, PdPt-2 NWs exhibited the highest ECSA in Figs. S14 and S15 (Supporting information), which effectively enhanced their electrocatalytic performance for HER. Stability is another crucial factor for electrocatalysts, and PdPt-2 NWs demonstrated superior durability compared to Pt/C during the accelerated durability test (ADT) across the full pH range in Fig. S16 (Supporting information). Additionally, PdPt-2 NWs were evaluated using chronopotentiometry at 200 mA/cm$^2$ current densities, revealing negligible current density decay after HER operation, whereas Pt/C exhibited a significant decline in current density (Fig. S17 in Supporting information). Compared with previously reported studies summarized in Table S3 (Supporting information), these results further imply that the Pt-Pd alloy composition plays a key role in enhancing HER activity. As demonstrated in Fig. S18 (Supporting information), the LSV curves following ECSA normalization illustrate the remarkable intrinsic activity of the PdPt-2 NWs electrocatalyst. To explore the structural stability of PdPt NWs, the TEM was also tested after the catalytical operation. From Fig. S19 (Supporting information), PdPt-2 NWs still present nanowires and have good stability under harsh electrochemical conditions, confirming the excellent stability. As shown in Fig. S20 (Supporting information), the PdPt phase structure of PdPt-2 NWs remained unchanged after the stability test, confirming its outstanding stability. XPS spectra of PdPt-2 NWs after catalysis also revealed that Pd and Pt peaks did not shift in Fig. S21 (Supporting information). These above results indicated that PdPt-2 NWs maintained its physical structure and chemical stability after harsh HER operation. Furthermore, PdAu NWs, PdIr NWs, and PdRu NWs were also evaluated for their HER activity in both acidic, alkaline and neutral environments. As illustrated in Fig. S22 (Supporting information), the results demonstrate that Pd-based alloy nanowires exhibit excellent performance for HER, especially PdPt NWs demonstrated the highest activity due to their intrinsic properties. The ultrathin nanowire structure enhances the exposure of active sites, while the alloying of Pd with Pt, Au, Ir, and Ru disrupts the electronic equilibrium and shifts the d-band center upward, thereby optimizing the adsorption of reaction intermediates. The synergistic effect of Pd and Pt significantly optimizes the electronic structure characteristics of the active sites in the PdPt alloy, making them closer to the ideal value of the hydrogen adsorption free energy ($\Delta G_H$). Furthermore, the surface strain effect introduced in the PdPt alloy could adjust the metal bond and redistribute the electron density, thereby further optimizing the hydrogen adsorption energy. These factors work together to significantly enhance the HER performance of the PdPt alloy, making it superior to pure Pt and pure Pd. The HER activity of PdPt-2 NWs catalysts were also studied using density functional theory (DFT). Models were constructed for the PdPt (111), Pt (111) and Pd (111) surfaces (Figs. S23-S25 in Supporting information). The hydrogen adsorption free energy ($\Delta G_H$) on the PdPt-2 NWs was found to be lower than that on the pure Pt and pure Pd sites (Fig. 4A), indicating that the PdPt-2 NWs had a stronger binding energy with hydrogen and were more susceptible to HER [63,64]. This suggests that the PdPt-2 NWs catalysts were more active for HER. Furthermore, the d-band centers of Pt and Pd in PdPt-2 NWs exhibited positive and negative shifts in comparison with their respective pure Pt and Pd counterparts (Fig. 4B), thereby suggesting the pres-

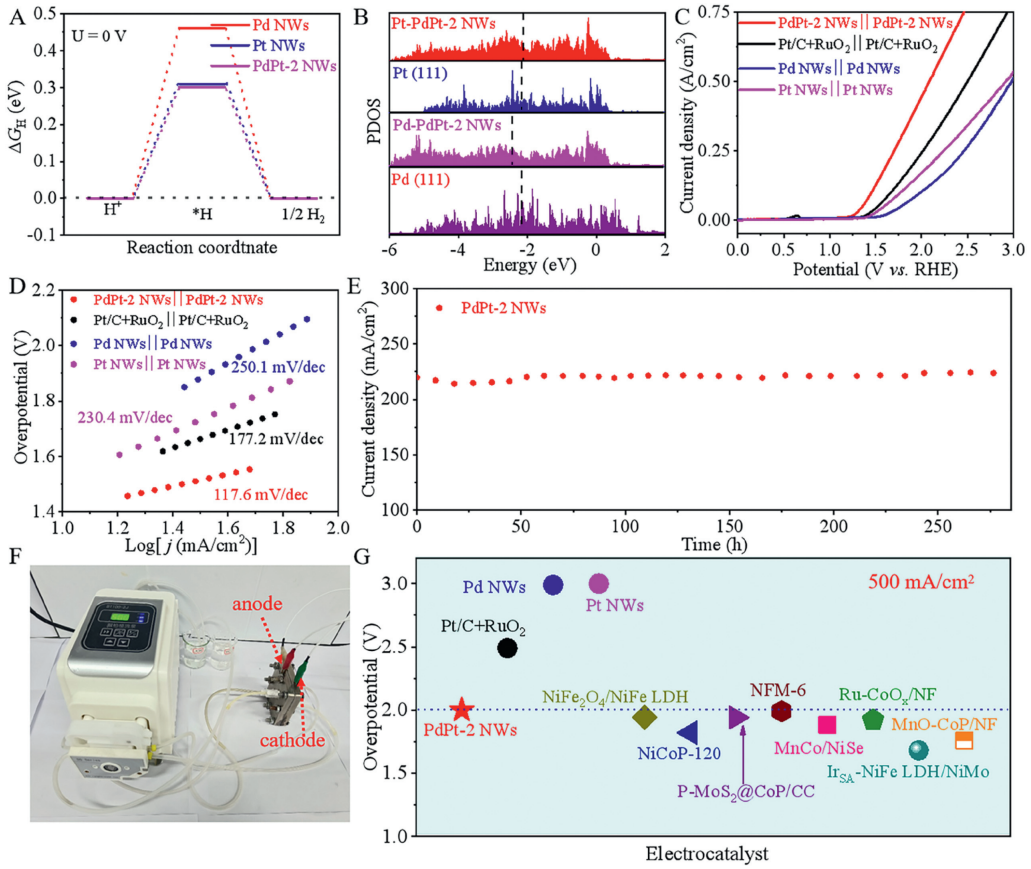



**Fig. 4.** (A) $\Delta G_H$ values on PdPt-2 NWs, Pt NWs, and Pd NWs. (B) pDOSs of Pt 5d and Pd 4d in PdPt-2 NWs, Pt (111), and Pd (111) (each d-band center is marked by a dashed line) with the Fermi level aligned at 0 eV. (C) LSV curves of PdPt-2 NWs||PdPt-2 NWs, Pd NWs||Pd NWs, Pt NWs||Pt NWs and Pt/C+$RuO_2$||Pt/C+$RuO_2$ for water splitting in 1 mol/L KOH. (D) Tafel slope in 1 mol/L KOH. (E) Chronoamperometric plots of PdPt-2 NWs for water splitting in 1 mol/L KOH at 220 mA/cm$^2$. (F) Configuration of AEM water electrolyzer for PdPt-2 NWs||PdPt-2 NWs in 1 mol/L KOH. (G) Comparison of required potentials for water splitting in alkaline electrolyte at 500 mA/cm$^2$.

ence of electronic interactions between Pt and Pd to enhance the activity of HER in PdPt-2 NWs [65].

PdPt NWs were also evaluated for OER activity. As shown in Fig. S26 (Supporting information), PdPt-2 NWs exhibited superior electrocatalytical activity compared to that of $RuO_2$ in acidic, alkaline, and neutral environments. Encouraged by their excellent HER and OER activities of PdPt-2 NWs, a two-electrode electrolyser was constructed with PdPt-2 NWs as both the anode and cathode to assess the overall water splitting performance. As illustrated in Fig. S27A (Supporting information), water splitting was initially conducted under acidic conditions, wherein PdPt-2 NWs||PdPt-2 NWs demonstrated the lowest overpotential of 1.76 V at 200 mA/cm$^2$, which was lowest than that of Pt/C||$RuO_2$ (1.87 V), Pt NWs||Pt NWs (2.36 V) and Pd NWs||Pd NWs (2.64 V) in 0.5 mol/L $H_2SO_4$. In contrast, PdPt-2 NWs (120.2 mV/dec) displays lower Tafel slopes in comparison to Pd NWs (308.3 mV/dec), Pt NWs (206.0 mV/dec) and Pt/C (187.3 mV/dec) (Fig. S27C in Supporting information). As illustrated in Fig. 4C, PdPt-2 NWs||PdPt-2 NWs requires a relatively lower cell voltage of 1.62 V at a current density of 200 mA/cm$^2$ compared to that of Pt/C||$RuO_2$ (1.91 V), Pt NWs||Pt NWs (2.28 V) and Pd NWs||Pd NWs (2.54 V) in 1 mol/L KOH, indicating the superior activity of PdPt-2 NWs for overall water splitting. Tafel slopes for PdPt-2 NWs, Pd NWs, Pt NWs and Pt/C catalysts were determined to be 117.6 mV/dec, 250.1 mV/dec, 230.4 mV/dec, and 177.2 mV/dec in Fig. 4D, respectively. The results demonstrate that PdPt-2 NWs facilitate accelerated kinetics for electrocatalytic water splitting. To improve practical applicability, the optimized PdPt-2 NWs were employed as the cathode in the anion exchange membrane (AEM) alkaline water electrolyzer in 1 mol/L KOH. PdPt-2 NWs exhibited remarkable stability, maintaining a long-term water-splitting performance for 280 h at a current density of 220 mA/cm$^2$ without obvious degradation (Fig. 4E), which was integrated with gas collection and recirculation systems in Fig. 4F. The Faradic efficiency of PdPt-2 NWs was also measured through the water drainage method (Fig. S28 in Supporting information), the volume of $H_2$ and $O_2$ were quantitatively collected in the alkaline electrolyzer in Fig. S29 (Supporting information). The corresponding volume-time curve exhibits that the volume ratio of collected $H_2$ and $O_2$ is about 1.95:1 in Fig. S30 (Supporting information), which is similar to the theoretical ratio of 2:1 for the water splitting. FE of PdPt-2 NWs for water splitting is estimated to be 100 %, suggesting PdPt-2 NWs could serve as a candidate electrocatalyst for the water splitting. Compared to the previously reported electrocatalysts in Fig. 4G and Table S4 (Supporting information), PdPt-2 NWs stands out as a promising catalyst for the water splitting application in alkaline electrolyte. Furthermore, the water splitting performance of PdPt-2 NWs||PdPt-2 NWs was assessed in 1 mol/L PBS (Figs. S27B and D in Supporting information), respectively. PdPt-2 NWs also have excellent activity exceptional stability for overall water splitting in neutral conditions.

In conclusion, we have introduced a straightforward wet-chemical method to synthesize a series of Pd-based alloy NWs, which exhibit excellent electrocatalytic activity and stability, including PdPt NWs, PdAu NWs, PdIr NWs, and PdRu NWs. Among these catalysts, PdPt NWs have excellent performance activity and stability for water splitting at full pH range. PdPt NWs could provide highly increased active sites and a finely tuned electronic configuration, thereby enhancing the reaction kinetics and water split-

ting electrocatalysis. This fabrication strategy could produce ultrathin Pd-based alloy nanowires served as high-performance electrocatalysts for water-splitting applications.

## Declaration of competing interest

The authors declare that they have no known competing financial interests or personal relationships that could have appeared to influence the work reported in this paper.

## CRediT authorship contribution statement

**Yuanwei Ma:** Writing – original draft, Investigation, Formal analysis. **Jigang Wang:** Resources, Investigation, Formal analysis. **Zhaodi Yan:** Investigation, Formal analysis. **Qiang Liu:** Methodology, Investigation. **Lanyan Li:** Writing – original draft, Visualization, Supervision. **Zhongfang Li:** Supervision, Project administration, Conceptualization. **Likai Wang:** Writing – review & editing, Writing – original draft, Supervision, Project administration, Methodology.

## Acknowledgments

L. Wang is grateful for the financial support from the National Natural Science Foundation of China (Nos. 21805170, 22172093), Natural Science Foundation of Shandong Province (Nos. ZR2023QB219, ZR2021QB161), and Qingdao Postdoctoral Innovation Project (No. QDBSH20220202031).

## Supplementary materials

Supplementary material associated with this article can be found, in the online version, at doi:10.1016/j.cclet.2025.111724.

## References

[1] T.H. Wang, L. Tao, X.R. Zhu, et al., Nat. Catal. 5 (2021) 66–73.
[2] Y.T. Ye, J.C. Xu, X.L. Li, et al., Adv. Mater. 36 (2024) e2312618.
[3] T.H. Zhao, M.T. Li, D.D. Xiao, et al., Angew. Chem. Int. Ed. 63 (2024) e202315148.
[4] P.Y. Kuang, Z.R. Ni, B.C. Zhu, Y. Lin, J.G. Yu, Adv. Mater. 35 (2023) 2303030.
[5] C. Chen, J.Y. Guo, J.H. Liu, et al., Chem. Commun. 59 (2023) 12863–12866.
[6] Q.Q. Mao, X. Mu, K. Deng, et al., Adv. Funct. Mater. 33 (2023) 2304963.
[7] Y.G. Sun, X. Du, J.G. Wang, et al., Rare Met. 43 (2024) 6447–6459.
[8] N. Wang, S.L. Ning, X.L. Yu, et al., Appl. Catal. B: Environ. 302 (2022) 120838.
[9] T. Wu, M.Z. Sun, B.L. Huang, Rare Met. 41 (2022) 2169–2183.
[10] A.X. Shan, X.A. Teng, Y. Zhang, et al., Nano Energy 94 (2022) 106913.
[11] J.P. Masnica, S. Sibt-e-Hassan, S. Potgieter-Vermaak, et al., Green Carbon 1 (2023) 160–169.
[12] B.Z. Lu, L. Guo, F. Wu, et al., Nat. Commun. 10 (2019) 631–641.
[13] Z.Y. Zhang, L.H. Li, Y.H. Li, et al., Chem. Eng. J. 469 (2023) 143846.
[14] S.D. Yu, J. Li, J.T. Yin, et al., Chin. Chem. Lett. 35 (2024) 216144.
[15] H.Y. Guo, L. Li, Y. Chen, et al., Adv. Mater. 35 (2023) 2302285.
[16] W. Zhang, X. Jiang, Z.M. Dong, et al., Adv. Funct. Mater. 31 (2021) 2107181.
[17] Q.N. Wang, Z.H. Tang, L.K. Wang, et al., Chem. Select. 1 (2016) 6044–6052.
[18] S.D. Yu, J. Li, Y.K. Du, et al., Coord. Chem. Rev. 520 (2024) 216144.
[19] S.D. Yu, N.N. Zhang, J. Li, et al., ACS Sustain. Chem. Eng. 12 (2024) 4551–4564.
[20] S.H. Gebre, Results Chem. 5 (2023) 100952.
[21] Y. Wang, J. Li, P.F. Yang, et al., J. Energy Chem. 102 (2025) 618–627.
[22] B.W. Zhou, J.P. Wang, L.F. Guo, et al., Adv. Energy Mater. 14 (2024) 2402372.
[23] M.Y. Zhang, B.W. Zhou, L.F. Guo, et al., Inorg. Chem. Front. 11 (2024) 5884–5893.
[24] T.B.N. Huynh, J. Song, H.E. Bae, et al., Adv. Funct. Mater. 33 (2023) 2301999.
[25] Y.C. Zhang, T.R. Yang, J. Li, et al., Adv. Funct. Mater. 33 (2023) 2210939.
[26] Y.Z. Lu, L.L. Tang, P. Wang, et al., ACS Catal. 13 (2023) 13804–13815.
[27] R. Li, M. Tursun, Y.J. Jiang, et al., ACS Mater. Lett. 5 (2023) 2384–2392.
[28] H.Z. Wang, P.F. Yang, X.Y. Sun, et al., J. Energy Chem. 87 (2023) 286–294.
[29] Z.P. Bao, C.Y. Li, L. Yan, Y.J. Ding, X.F. Wu, Green Carbon 2 (2024) 205–208.
[30] W.C. Li, N. Bhuvanendran, H.Y. Liu, et al., J. Alloys Compd. 933 (2023) 167706.
[31] W. Yan, Z.H. Tang, L.K. Wang, et al., Int. J. Hydrogen Energy 42 (2017) 218–227.
[32] H.Y. Yang, Z.H. Tang, W. Yan, et al., J. Alloys Compd. 702 (2017) 146–152.
[33] X.Y. Cui, Y.C. Liu, X.Y. Wang, et al., ACS Nano 18 (2024) 2948–2957.
[34] X.T. Yang, Q. Yuan, J.W. Li, et al., Nano Lett. 23 (2023) 3467–3475.
[35] Y. Shen, B. Gong, K.J. Xiao, L. Wang, ACS Appl. Mater. Interface 9 (2017) 3535–3543.
[36] J.G. Wang, G.Y. Zhang, H. Liu, L.K. Wang, Z.F. Li, Small 20 (2024) 2310277.
[37] H.G. Zhang, X.M. Li, Y.L. Wang, et al., Appl. Catal. B: Environ. 338 (2023) 123006.
[38] L. Huang, J. Yang, M. Wu, et al., J. Power Sources 398 (2018) 201–208.
[39] W.X. Wang, Q.Q. Mao, S.J. Jiang, et al., Appl. Catal. B: Environ. 340 (2024) 123194.
[40] H. Lv, X. Chen, D.D. Xu, et al., Appl. Catal. B: Environ. 238 (2018) 525–532.
[41] N.K. Qian, L. Ji, J.J. Li, H. Zhang, D.R. Yang, Nano Res. 16 (2023) 9125–9131.
[42] J.X. Tang, Q.S. Chen, L.X. You, et al., J. Mater. Chem. A 6 (2018) 2327–2336.
[43] C.R. Zanata, C.A. Martins, É. Teixeira-Neto, M.J. Giz, G.A. Camara, J. Catal. 377 (2019) 358–366.
[44] L.Z. Sun, B. Liu, Adv. Mater. 35 (2023) 2207305.
[45] Y. Wang, N. Gong, G. Niu, et al., J. Alloys Compd. 960 (2023) 171039.
[46] Z.M. Yang, N. Qiu, H.M. Yang, Y. Wang, J. Alloys Compd. 947 (2023) 169512.
[47] X. Jiang, Y.X. Xiong, R.P. Zhao, et al., Nano Res. 13 (2020) 2691–2696.
[48] M.F. Li, Z.P. Zhao, T. Cheng, A. Fortunelli, Science 354 (2016) 1414–1419.
[49] S.L. Liu, H. Ren, S.L. Yin, et al., Chem. Eng. J. 435 (2022) 134823.
[50] Y.S. Xu, D.X. Wu, P.L. Deng, et al., Appl. Catal. B: Environ. 308 (2022) 121223.
[51] J.W. Hu, R. Li, X. Wang, S.Z. Wang, C.H. Fang, ACS Appl. Nano Mater. 6 (2023) 10213–10222.
[52] B. Klebowski, M. Stec, J. Depciuch, et al., Cancers 14 (2022) 5899.
[53] G. Fisseha, Y.P. Hu, Y.N. Yu, et al., Chin. Chem. Lett. 35 (2024) 108445.
[54] W. Wang, X. Zhang, Y.H. Zhang, et al., Nano Lett. 20 (2020) 5458–5464.
[55] M. Wei, Y.Y. Sun, J.Y. Zhang, et al., Energy Environ. Sci. 16 (2023) 4009–4019.
[56] C.H. Fang, J. Zhao, R.B. Jiang, et al., ACS Appl. Mater. Interface. 10 (2018) 29543–29551.
[57] T.T. Guo, H.Y. Xiang, W. Li, et al., ACS Sustain. Chem. Eng. 8 (2020) 2901–2909.
[58] L.H. Jin, Z.H. Zhang, Z.H. Zhuang, et al., RSC Adv. 6 (2016) 42008–42013.
[59] W.T. Koo, Y. Kim, S. Kim, et al., Chem 6 (2020) 2746–2758.
[60] C.H. Wang, J. Zhang, K.H. Miao, et al., Adv. Mater. 36 (2024) 2400433.
[61] L.Y. Zhu, D.D. Xu, C.L. Yi, Chem. Commun. 59 (2023) 13978–13981.
[62] T.T. Yang, T.L. Tan, W.A. Saidi, Chem. Mater. 32 (2020) 1315–1321.
[63] W.H. Lai, L.F. Zhang, W.B. Hua, et al., Angew. Chem. Int. Ed. 58 (2019) 11868–11873.
[64] R.Q. Yan, J. Li, L.J. Zhao, et al., Nano Lett. 24 (2024) 4849–4857.
[65] H. Zhang, Q.F. Jiang, J.H.L. Hadden, F. Xie, D.J. Riley, Adv. Funct. Mater. 31 (2020) 2008989.